A comparison of survey-grade GNSS receivers by means of observation and coordinate domain approaches; traditional vs low-budget

Ola ØVSTEDAL, Johan Tobias ARNELL, Isak Foss INGEBRIGTSEN, Simen Walbækken TANGEN and Bjørn-Eirik ROALD, Norway

Key words: GNSS, receiver characterization, low-cost receivers, kinematic GNSS, raw-data quality, cross-track errors.

SUMMARY

In recent years, several low-cost GNSS receivers have entered the market. The specifications of some of these low-cost receivers seem to match the specifications of more expensive receivers from traditional manufactures. In the present work, we compared a low-cost GNSS receiver to a traditional state-of-the-art GNSS receiver. The combined effect of multipath and noise on code observations and the ability to maintain lock on carrier phase observations have both been evaluated using a geometry-free observation domain approach. Based on kinematic measurements of a reference trajectory, we have compared the two receivers' capability when used in network Real Time Kinematic (RTK) mode and in Precise Point Positioning (PPP) based on post-processing. The low-cost receiver supplies dual-frequency observations to only 75% of all GPS-satellites due to lacking P(Y)-code tracking capabilities (as of autumn 2021). Also, the low-cost receiver experienced significantly more cycle-slips than the traditional receiver. We did however verify that many of the apparent cycle slips in carrier phase observations from the low-cost receiver were not due loss of lock of the GNSS-signal but rather a recording/storage issue. The low-cost receiver did not perform as well as the traditional receiver in kinematic PPP using GPS and GLONASS only. When used in kinematic network RTK using GPS, GLONASS, Galileo and BeiDou, there were only small differences between the two receivers.

A comparison of survey-grade GNSS receivers by means of observation and coordinate domain approaches; traditional vs low-budget

Ola ØVSTEDAL, Johan Tobias ARNELL, Isak Foss INGEBRIGTSEN, Simen Walbækken TANGEN and Bjørn-Eirik ROALD, Norway

1. INTRODUCTION

State-of-the-art multi-system, multi-frequency and multi-signal GNSS receivers used in e.g. navigation or geodesy have until recently been relatively expensive. In recent years, new companies have entered the market offering receivers with considerably lower price tags than traditional receivers. The specifications of some of these new low-cost receivers seem to match the specifications of traditional state-of-the-art receivers.

Previously, FIG Commission 5 has published detailed reports concerning cost-effective GNSS. FIG publication 49 (Weston & Schwieger, 2010) gives a thorough introduction to the general principles of GNSS, its error sources and its different positioning techniques. This publication proposes the use of low-cost GNSS receivers as an alternative to high-end geodetic receivers. The use of Continuously Operating Reference Stations (CORS) to aid such receivers is also suggested. FIG publication 74 (Lipatnikov & Shevchuk, 2019) expands on FIG publication 49 by detailing many of the options available for reducing the cost of receiver hardware. The authors suggest, among other things, the use of low-cost and ultra-low-cost GNSS chips in high-precision position devices. Furthermore, the use of free open-source GNSS software or free online post-processing services is proposed as an alternative to commercial processing software.

In the current work, a representative of a low-cost multi-system, multi-frequency and multi-signal GNSS receiver, namely an Emlid Reach RS2, is compared to a representative of a traditional high-end state-of-the-art GNSS receiver, namely a Topcon HiPer VR. In the comparison we first give a short summary of specifications that are of special interest for positioning and navigation. Next, we focus on completeness and quality of code and carrier phase observations, and on the performance of receivers when used in kinematic positioning of trajectories.

To quantify completeness and quality of observations, we have collected one static and two kinematic sets of observations. Each data set was collected using both receivers simultaneously while they were closely co-located. Raw code and carrier phase observations were analyzed in a geometry-free observation domain to identify cycle slips in carrier phase observations and the combined effects of noise and multipath on code observations. In a pre-survey, the coordinates of 22 well-defined control points along a reference trajectory were estimated using static network RTK-observations in a post processed least-squares adjustment. The coordinates of the control points served as ground truth for the evaluation of kinematic trajectories estimated using the two receivers.

Section 2 outlines the approach we have chosen to quantify the quality of raw code and carrier phase observations in a geometric-free observation domain as well as the accuracy of kinematic

trajectories in a geometry-dependent coordinate domain. In Section 3, we present relevant specifications for the two receivers. Field work and kinematic PPP post-processing are described in section 4. Processing and analysis are presented in section 5, while conclusions are drawn in Section 6.

2. QUALITY NUMBERS IN OBSERVATION AND IN COORDINATE DOMAINS

2.1 Evaluation using an observation domain approach

Code and carrier phase observations can both be interpreted as pseudorange observations between a satellite at the time of signal emission and a receiver at the time of signal reception (Hofmann-Wellenhof, et al., 2008).

Denoting code observation with P and carrier phase observation with ϕ, simplified models for the observations are given by:

$$P_i = \rho + c(dt - dT) + I_i + T + MP_i, \quad (1)$$

$$\phi_i = \rho + c(dt - dT) - I_i + T + N_i\lambda_i + M\phi_i. \quad (2)$$

ρ is the geometric distance between a satellite at the time of signal emission and a receiver at the time of signal reception, c is the speed of light, dt and dT are the receiver and satellite clock errors respectively, I_i is the ionospheric delay, T is the tropospheric delay, MP_i and $M\phi_i$ are the multipath effects on code and carrier phase respectively, N_i is the carrier phase ambiguity and λ_i is the wavelength of the carrier phase signal. Index i is used to assign the frequency of the carrier phase signal. E.g. for the GPS-system, i=1 or i=2 implies the use of f_1=1575.42 MHz or f_2=1227.60 MHz. Most GNSS systems transmit signals at three different frequencies; i=1,2,3.

Since terms like relativistic effects, code and carrier phase hardware delays in satellite and receiver, carrier phase wind-up and noise in code and carrier phase observations are not relevant for our approach to quantification of quality numbers, they are omitted in equations 1 and 2. However, it must be mentioned that carrier phase observations are much more precise than code observation, by approximately two orders of magnitude in terms of standard deviations.

We notice the inclusion of $N_i\lambda_i$ in Equation 2 to account for the ambiguity of the carrier phase observable and that the ionospheric term has an opposite sign for code and carrier phase.

The first order ionospheric delay at frequency f_i is given by (e.g. Hofmann-Wellenhof et al., 2008):

$$I_i = \frac{40.3}{f_i^2}\, TEC, \quad (3)$$

where TEC is the integral of the electron density along the ray path between satellite and receiver. TEC provides the number of electrons per square meter and is usually given in units where one TEC unit (TECU) is $10^{16}\ m^{-2}$.

As seen in Equation 3, the ionospheric delay is inversely proportional to the square of the carrier frequency. Hence, the ionospheric delay at frequency f_i, i=2,3, can be expressed as a function of the delay at the f_1-frequency.

$$I_i = \propto_i I_1, \qquad \propto_i = \frac{f_1^2}{f_i^2} \tag{4}$$

It is readily seen that ionospheric delay can be estimated from dual-frequency observations. Subtracting carrier phase observations given by Equation 2 using f_1 and f_i frequencies, we obtain:

$$I_1 = \frac{(\phi_1 - \phi_i)}{(\propto_i - 1)} - \frac{(N_1\lambda_1 - N_i\lambda_i)}{(\propto_i - 1)} - \frac{(M\phi_1 - M\phi_i)}{(\propto_i - 1)}. \tag{5}$$

The estimated ionospheric delay can now be treated as a correction term. Starting with the carrier phase observations on the f_1-frequency seen in Equation 2, then inserting Equation 5 for I_1 and moving this term to the left-hand side, we obtain the ionosphere-free linear combination of carrier phase observations; ϕ_{IF}.

$$\overbrace{\phi_1 + \frac{(\phi_1 - \phi_i)}{(\propto_i - 1)}}^{\phi_{IF}} = \rho + c(dt - dT) + T + \left[N_1\lambda_1 + \frac{(N_1\lambda_1 - N_i\lambda_i)}{(\propto_i - 1)}\right] + \left[M\phi_1 + \frac{(M\phi_1 - M\phi_i)}{(\propto_i - 1)}\right] \tag{6}$$

The terms in brackets on the right-hand side of Equation 6 account for the total effect of biases due to ambiguities of the carrier phase observations, and for multipath on carrier phase observations.

We now adopt the approach used by Estey&Merteens, 1999. The starting point is the knowledge that carrier phase observations are two orders of magnitude more precise than code observations. Similarly, multipath on carrier phase observations is considered negligible compared to multipath on code observations.

Using the f_1-frequency, code observations given by Equation 1 are corrected for ionospheric delay given by Equation 5. Ionosphere-free carrier phase observations are then subtracted from the corrected code observations to obtain multipath on code observations.

$$(P_1 - I_1 - MP_1) - \phi_{IF} = 0 \tag{7}$$

Inserting equations 1, 5 and 6 into Equation 7 gives us the estimated code multipath on the f_1-frequency.

$$MP_1 = P_1 - \left(1 + \frac{2}{\propto_i - 1}\right)\phi_1 + \left(\frac{2}{\propto_i - 1}\right)\phi_i + B_1 + MP\phi_1 \tag{8}$$

B_1 is a bias term due to carrier phase ambiguities and $MP\phi_1$ is due to multipath on carrier phase observations;

$$B_1 = \left(1 + \frac{2}{\propto_i - 1}\right) N_1\lambda_1 - \left(\frac{2}{\propto_i - 1}\right) N_i\lambda_i, \tag{9}$$

$$MP\phi_1 = \left(1 + \frac{2}{\propto_i - 1}\right) M\phi_1 - \left(\frac{2}{\propto_i - 1}\right) M\phi_i. \tag{10}$$

For other frequencies f_i , i=2,3, similar operations yield:

$$MP_i = P_i - \left(\frac{2 \propto_i}{\propto_i - 1}\right)\phi_1 + \left(\frac{2 \propto_i}{\propto_i - 1} - 1\right)\phi_i + B_i + MP\phi_i, \tag{11}$$

with bias term B_i and carrier phase ambiguity term $MP\phi_i$:

$$B_i = \left(\frac{2 \propto_i}{\propto_i - 1}\right) N_1\lambda_1 - \left(\frac{2 \propto_i}{\propto_i - 1} - 1\right) N_i\lambda_i, \tag{12}$$

$$MP\phi_i = \left(\frac{2 \propto_i}{\propto_i - 1}\right) M\phi_1 - \left(\frac{2 \propto_i}{\propto_i - 1} - 1\right) M\phi_i. \tag{13}$$

In the following, the carrier phase multipath terms $MP\phi_1$ and $MP\phi_i$ are considered small enough to be neglected. The bias terms, B_1 and B_i, remain constant as long as there are no cycle slips in the carrier phase observations. To identify eventual cycle slips, we monitor the continuity in time-series of ionospheric delays computed using Equation 5. Sudden jumps in ionospheric delay from epoch to epoch that cannot be explained by ionospheric time-variation, are used as indicators of cycle slips, see e.g. Hofmann-Wellenhof et al., 2008 and Estey&Merteens, 1999. For each satellite and continuous arc of carrier phase observations, j, we estimate average bias terms:

$$\hat{B}_{1,j} = \frac{\sum_{k=1}^{n_j}(MP_1)_k}{n_j} \qquad \hat{B}_{i,j} = \frac{\sum_{k=1}^{n_j}(MP_i)_k}{n_j}, \tag{14}$$

where k is the epoch number and n_j is the number of epochs in arc j. Each cycle slip will introduce a new arc, j, with associated bias term. Standard deviations for MP_1 and MP_i for each satellite is computed as the square root of the sum of all squared differences between average bias terms and epoch-wise code multipath divided by total number of epochs minus the number of arcs.

$$s_{MP1} = \sqrt{\frac{\sum_{j=1}^{n_{arc}}\sum_{k=1}^{n_j}\left(\hat{B}_{1,j} - (MP_1)_k\right)^2}{n_{tot} - n_{arc}}} \qquad s_{MPi} = \sqrt{\frac{\sum_{j=1}^{n_{arc}}\sum_{k=1}^{n_j}\left(\hat{B}_{i,j} - (MP_i)_k\right)^2}{n_{tot} - n_{arc}}} \tag{15}$$

In Equation 15 n_{tot} is the total number of epochs used in the computations and n_{arc} is the number of continuous arcs.

It should be noted that the estimates of code multipath, as described above, constitute the combined effect of both multipath and noise on the respective code observables. This combined effect is directly linked to positioning using code observations. In high-precision applications using carrier phase as the main observables, the quality of code observations is in most approaches important to preprocessing and carrier phase ambiguity fixing.

Another important property of a receiver is the ability to provide continuous carrier phase observations. Signal degradation due to e.g. physical obstructions or ionospheric irregularities as well as faults in receiver hardware and firmware can cause loss of lock of a GNSS signal. In this work, we have used the total number of cycle slips as well as the relative number of cycle slips as measures of the two receivers' ability to maintain lock on carrier phase observables.

For each GNSS-system, we estimated code multipath for the first frequency, $MP1$, and for the second frequency, $MP2$, using observations on respective frequencies. Code multipath for the third frequency, $MP3$, can be estimated using observations on the first and the third frequency. Cycle slips were detected using the approach described previously.

2.2 Evaluation using a coordinate domain approach

To evaluate kinematic positioning capabilities, both receivers were simultaneously set into operation in kinematic mode along an approximately 5 km long reference trajectory, see Figure 1.

Along the reference trajectory, 22 control points had been pre-marked. The control points have very different characteristics with regards to physical obstruction from buildings, terrain and vegetation. At each point, we carried out 30 seconds of static network RTK-observations, with "fixed carrier phase ambiguity status". These measurements were repeated on two other days for a total of three independent measurements of each point. The Topcon HiPer VR GNSS receiver received network RTK-corrections from the CPOS service operated by the Norwegian Mapping Authority (Kartverket, 2021). In CPOS, the NTRIP protocol is used to stream Virtual Reference Station (VRS) corrections in RTCM-format. Corrections are referred to the Norwegian reference frame EUREF89 and supplied for observations from GPS, GLONASS, Galileo and BeiDou. Coordinates from the static RTK-measurements, were imported as observations in the least-squares adjustment module of the GISLINE software (Norkart, 2021). Based on statistic testing using the multiple t-test approach, 4 observations, out of 66, were identified as outliers and rejected. After carrying out supplemental observations, all 22 points were associated to at least three observed days. Final horizontal coordinates of control points were estimated with standard deviations smaller than 0.01 m and external reliabilities smaller than 0.02 m.

When carrying out kinematic measurements, both GNSS-antennas passed directly over each of the 22 control points at a walking speed of approximately 1.5 m/s. The recording interval in the receivers was 1 second, and we did not apply any device to time-tag when the respective antennas passed each control point. As it then is not possible to directly compare coordinates from the kinematic positionings with the coordinates of the control points, we have adopted a one-dimensional cross-track error approach to the evaluation in a coordinate domain. Horizontal north/east coordinate differences, between the control point and closest point in the GNSS-trajectory, are rotated into a platform-fixed coordinate system with the x-axis along the trajectory and the y-axis perpendicular to the trajectory. Coordinate differences in the y-direction then give cross-track errors. A cross-track error can be interpreted as the shortest horizontal distance between each control point and the respective GNSS-trajectory. The sign of a cross-track error gives information on whether a GNSS-trajectory passes to the right or the left of a control point.

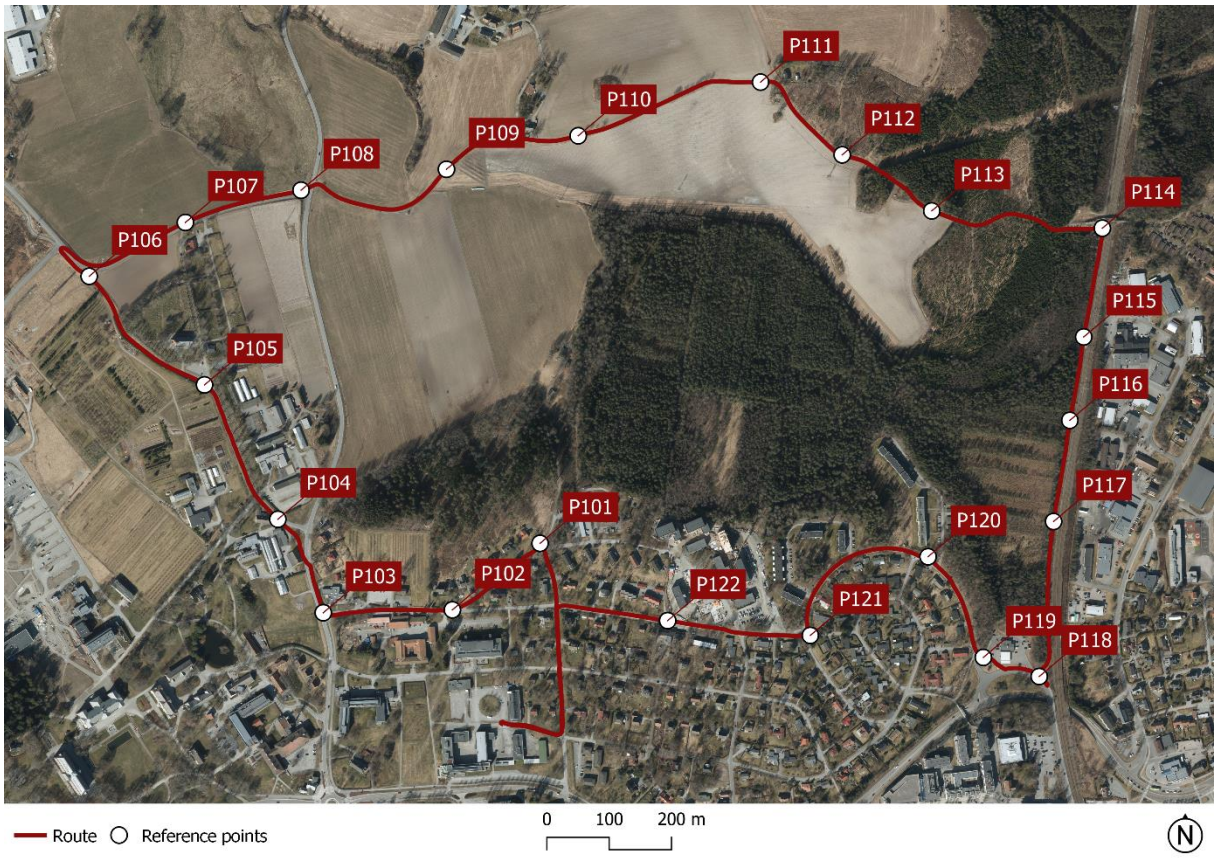

Figure 1. Ortophoto over reference trajectory and control points.

3. GNSS-RECEIVER SPECIFICATIONS

The price tag of the Topcon HiPer VR receiver is approximately one order of magnitude higher than the price tag of the Emlid Reach RS2 receiver (Roald, 2020). We do not give a full

description of all general specifications and capabilities of the two receivers but instead focus on tracking of signals from the four GNSS-systems GPS, GLONASS, Galileo and BeiDou and on performance in kinematic positioning using RTK and PPP.

For general description of the Emlid Reach RS2 receiver, we refer to GPS-World, 2019, and to official information given by Emlid (Emlid, 2021). Although there is sparse information regarding the actual GNSS hardware, several sources (e.g. Emlid Community, 2021) indicate the implementation of the third-party GNSS-module ZED-F9P from company u-blox (u-blox, 2021). The Emlid receiver comes with an integrated patch antenna. The RTK processing engine is based on the open source RTKLIB software (Takasu, 2011).

Likewise, we refer to the official information given by Topcon (Topcon, 2021) for general information regarding the Topcon HiPer VR receiver. The Topcon receiver comes with an integrated micro-center Fence antenna with internal ground plane. The RTK-processing engine is a Topcon in-house software implementation.

For both receivers, the GNSS-antenna is integrated with the receiver. Specifications regarding GNSS systems and signals being tracked by the two receivers are given in Table 1. In Table 1 there is one row for each frequency of the four GNSS-systems.

Table 1. Receiver specifications for tracking of signals from GPS, GLONASS, Galileo and BeiDou. For each receiver, there is one row for each frequency.

Receiver	GPS	GLONASS	Galileo	BeiDou
Emlid Reach RS2	L1 C/A L2C	L1 C/A L2 C/A	E1 E5B	B1 B2
Topcon HiPer VR	L1 C/A, L1C L2P(Y), L2C L5	L1 C/A, L1P L2 C/A, L2 P L3	E1 E5A E5B	B1 B2

We notice that the Topcon-receiver, like most traditional high-end receivers, has implemented anti-spoofing technology to track the encrypted P(Y)-code broadcasted by the GPS satellites. The Topcon receiver then provides observations on the GPS f_2-frequency for all available satellites. The Emlid-receiver, however, relies on the modernized L2C-signal that are only broadcast by newer satellites. Currently (as of autumn 2021), 23 out of 31 GPS satellites broadcast the L2C-signal (GPS.GOV, 2021), meaning that the Emlid receiver only receives dual-frequency observations from 75% of all GPS-satellites.

Furthermore, the Topcon Receiver has the theoretical capability to supply observations on three frequencies for the GPS, GLONASS and Galileo systems. Upon inspecting our files with raw-observation in RINEX-format (IGS, 2021-a), we discovered that neither GPS L5 nor GLONASS L3 observations were present in the files, meaning that the Topcon-receiver supplied triple-frequency observations for the Galileo system only.

To sum up, the Topcon-receiver supplied dual frequency observations for GPS, GLONASS and BeiDou and triple-frequency observations for Galileo. The Emlid receiver supplied dual-frequency observations for GLONASS, Galileo, Beidou and for 75% of GPS satellites.

4. FIELD WORK AND PPP POST-PROCESSING

In this work we attempt to address the total performance of combined GNSS receiver and antenna systems. The two receivers, therefore, collected data using their respective integrated GNSS antennas. To ensure as similar conditions as possible, the receivers were closely co-located, with a between-receiver distance of approximately 0.70 m. On three different days, observations from satellites with elevation angles greater than 10 degrees were logged with a 1 Hz sampling rate using both the Emlid and the Topcon receiver, simultaneously.

On day 28.10.2021 we collected two hours of static observations in a station with a close to perfect open view. The station is located in an open field, approximately 50 meters west of control point P103, see Figure 1. The static dataset was used in the observation domain approach, as described above, to compare the two receivers under near ideal conditions.

On days 19.10.2021 and 21.10.2021 the two receivers operated in kinematic mode along the reference trajectory. For the kinematic datasets, we carried out analyses based on both the observations domain and the coordinate-domain approach.

During the kinematic measurements, we used a modified bike as a platform, see Figure 2. The two receivers, with integrated antennas, were mounted on a horizontal beam that was aligned with the along-track axis of the bike. Moving in a straight line, the two wheels of the bike defined the along-track axis. A level tube strapped to a vertical beam, carrying the horizontal beam, was used to minimize cross-track errors when the platform rolled over each pre-marked control point. During the surveys, one person walked the bike holding the handlebars while a second person ensured vertical alignment of the antennas by visually monitoring the level tube and applying eccentricity corrections via a support rod mounted at the rear of the bike. The observation platform moved with a uniform walking speed of approximately 1.5 m/s throughout each session.

Prior to the kinematic measurements, a calibration and verification scheme was carried out. With the use of a survey-grade theodolite, antenna cross-track eccentricity and alignment errors were minimized in a static calibration. To quantify typical cross-track eccentricity errors during operational kinematic surveys, the theodolite observed both the antennas and a control point from behind while the platform passed over a well-defined control-point. Based on 35 independent readings, the standard deviation of the cross-track eccentricity error was estimated to be $s_{ct\_ecc} = 0.04\ m$.

During the kinematic measurements, both receivers operated in network RTK-mode receiving network RTK-corrections from the CPOS-network, see above for information regarding CPOS.

The two receivers also simultaneously logged raw data in proprietary ubx- and tps-format for the Emlid and the Topcon receiver respectively. Files with raw-data were converted to RINEX-format for subsequent post-processing.

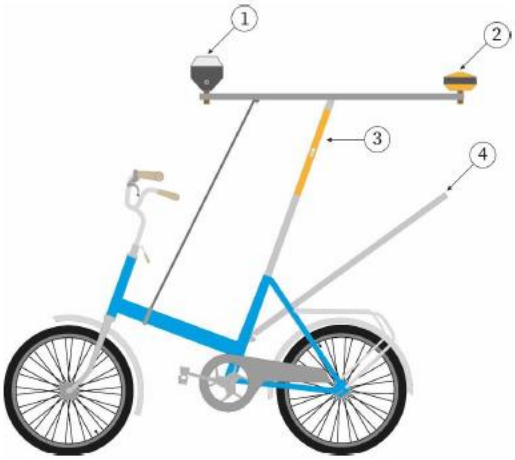

Figure 2. Measuring platform. (1) is the Emlid Reach RS2 receiver, (2) is the Topcon HiPer VR receiver, (3) is a tube level, (4) is a support rod to manually keep vertical alignment in cross-track direction.

Kinematic PPP processing was carried out by submitting the kinematic RINEX-files to the Canadian Spatial Reference System-PPP (CSRS-PPP) online service (Tétreault et al., 2005, Natural Resources Canada, 2021). The online CSRS-PPP service carries out PPP post-processing using dual-frequency code and carrier phase observations from GPS and GLONASS. Receiver antenna calibration parameters for both the Emlid and the Topcon antenna are supplied by the International GNSS Service (IGS, 2021-b), and are applied in the CSRS-PPP processing. Correct antenna identification information was inserted into the headers of RINEX observations files before submitting to PPP processing.

Coordinates estimated by PPP are referred to the last version of the International Terrestrial Reference Frame (ITRF), currently ITRF2014, at the epoch of observations. Before comparison with coordinates of control points, coordinates from the PPP-processing were transformed to the Norwegian reference frame EUREF89 using a PROJ software implementation supplied by the Norwegian Mapping Authority (Himle, 2021).

5. PROCESSING AND ANALYSES

We computed quality numbers based on analyses in the geometry-free observation domain and the geometry-dependent coordinate-domain using the approaches described in Section 2.

5.1 Geometry-free observation domain

An in-house MATLAB software (Roald, 2020) was used to process RINEX-files from the static and the two kinematic datasets. Only epochs and satellites with corresponding dual frequency

code and carrier phase observations were used in the processing meaning that e.g. single frequency observations were filtered out.

Extracts of quality numbers are given in Table 2 for the static dataset and in tables 3 and 4 for the kinematic datasets. In these tables, n_sat is the number of satellites with dual-frequency observations, n_obs is the total number of valid dual-frequency observations, s_{MP1} is the overall standard deviation for multipath on the first frequency, s_{MP2} is the overall standard deviation for multipath on the second frequency, n_slip is the number of cycle slips and rel_slip is the relative number of cycle slips in percent.

For the static dataset, we notice that the Emlid receiver provides dual-frequency code and carrier observations to fewer GPS satellites than the Topcon receiver. The Emlid receiver's lack of capability to track signals on the f_2-frequency for the older generation of GPS-satellites, see Section 3, is also reflected in that total number of valid dual-frequency GPS-observations is lower than for Topcon. Given that the static dataset was collected under near ideal conditions, both the total and the relative number of detected cycle slips are higher than expected for the Emlid receiver. Upon manual inspection of the computed ionospheric delay (Equation 5) and corresponding RINEX-file, we disclosed that observations for some satellites occasionally were missing for the Emlid receiver. When observations to the missing satellites reappeared in the RINEX-file, the computed ionospheric delays were very close to the corresponding ionospheric delays computed at the last valid epoch with observations, indicating that no cycle slip had taken place. As a result, it is likely that the source of these missing observations is not a signal tracking issue, but rather a data recording and storage issue. Most software for post-processing of these Emlid RINEX-files will however probably interpret occasionally missing observations as cycle slips.

Table 2. Results from observation domain analyses from static dataset 28.10.2021. n_sat is the number of satellites with dual-frequency observations, n_obs is the total number of valid dual-frequency observations, s_{MP1} is the overall standard deviation for multipath on the first frequency, s_{MP2} is the overall standard deviation for multipath on the second frequency, n_slip is the number of cycle slips and rel_slip is the relative number of cycle slips in percent.

Static 28.10.2021		GPS	GLONASS	Galileo	BeiDou
Emlid	n_sat	10	12	11	5
	n_obs	44149	45220	52423	28302
	s_{MP1} $[m]$	0.294	0.362	0.482	0.399
	s_{MP2} $[m]$	0.369	0.487	0.402	0.488
	n_slip	720	447	251	135
	rel_slip [%]	1.412	0.869	0.437	0.431
Topcon	n_sat	15	11	10	6
	n_obs	63361	47827	45681	38317
	s_{MP1} $[m]$	0.202	0.329	0.267	0.413
	s_{MP2} $[m]$	0.298	0.290	0.119	0.365
	n_slip	6	14	0	15
	rel_slip [%]	0.009	0.029	0.000	0.031

Table 3. Results from observation domain analyses from kinematic dataset 19.10.2021. n_sat is the number of satellites with dual-frequency observations, n_obs is the total number of valid dual-frequency observations, s_{MP1} is the overall standard deviation for multipath on the first frequency, s_{MP2} is the overall standard deviation for multipath on the second frequency, n_slip is the number of cycle slips and rel_slip is the relative number of cycle slips in percent.

Kinematic 19.10.2021		GPS	GLONASS	Galileo	BeiDou
Emlid	n_sat	8	11	9	2
	n_obs	21996	24709	24652	4048
	s_{MP1} $[m]$	0.309	0.361	0.500	0.297
	s_{MP2} $[m]$	0.324	0.415	0.268	0.300
	n_slip	1116	1463	1205	350
	rel_slip [%]	3.261	3.662	3.185	4.088
Topcon	n_sat	13	7	7	3
	n_obs	29706	22344	17420	6204
	s_{MP1} $[m]$	0.241	1.644	0.425	0.549
	s_{MP2} $[m]$	0.593	1.209	0.188	0.457
	n_slip	344	128	17	19
	rel_slip [%]	0.963	0.462	0.076	0.164

Table 4. Results from observation domain analyses from kinematic dataset 21.10.2021. n_sat is the number of satellites with dual-frequency observations, n_obs is the total number of valid dual-frequency , s_{MP1} is the overall standard deviation for multipath on the first frequency, s_{MP2} is the overall standard deviation for multipath on the second frequency, n_slip is the number of cycle slips and rel_slip is the relative number of cycle slips in percent.

Kinematic 21.10.2021		GPS	GLONASS	Galileo	BeiDou
Emlid	n_sat	10	10	10	5
	n_obs	21697	23440	22633	13066
	s_{MP1} $[m]$	0.232	0.303	0.400	0.303
	s_{MP2} $[m]$	0.350	0.334	0.241	0.299
	n_slip	1598	1544	1112	856
	rel_slip [%]	3.933	4.164	3.039	4.057
Topcon	n_sat	13	9	8	5
	n_obs	39725	25230	23662	17286
	s_{MP1} $[m]$	0.217	0.764	0.487	0.401
	s_{MP2} $[m]$	0.627	1.770	0.185	0.203
	n_slip	308	92	16	16
	rel_slip [%]	0.671	0.322	0.057	0.075

For s_{MP1} and s_{MP2} there are some apparent differences among the four GNSS system. However, errors due to multipath and noise on code observations will generally be elevation

angle dependent (e.g. Hofmann-Wellenhof et al., 2008). Our analyses are based on relatively short time spans, and the apparent differences in s_{MP1} and s_{MP2} values from one GNSS system to another might therefore be explained by differences in overall elevations angles.

We do however notice that for the static dataset, the Topcon receiver has lower numbers for code multipath than the Emlid receiver. For the kinematic datasets, however, the s_{MP2} numbers are higher for code observations from the Topcon receiver than for code observations from the Emlid receiver.

5.2 Geometry-dependent coordinate domain

Using coordinates of the 22 control points as ground truth, the approach described in Section 2 was used to compute cross-track errors, ε_{ct_i} , $i = 1,2, \ldots ,22$. For each receiver and dataset, we computed corresponding standard deviations:

$$s_{ct_{tot}} = \sqrt{\frac{\sum_{i=1}^{22}\left(\varepsilon_{ct_i}\right)^2}{22}}. \tag{16}$$

Assuming that GNSS specific errors are independent from eccentricity errors, when the receiver antennas passed over each control point, we computed adjusted standard deviations for cross-track errors, s_{ct}, with

$$s_{ct} = \sqrt{s_{ct_{tot}}^2 - s_{ct_{ecc}}^2}. \tag{17}$$

In Equation 17 $s_{ct_{tot}}$ is the standard deviation containing both GNSS specific errors and eccentricity errors, and $s_{ct_{ecc}}$ is standard deviation due to eccentricity errors. As described in Section 4, $s_{ct_{ecc}}$ was estimated to be 0.04 m.

Figure 3 shows cross-track errors, ε_{ct_i}, from the kinematic network RTK solutions while Figure 4 shows corresponding numbers from the post-processed PPP solutions.

Figure 3. Cross-track errors computed in each control point for the network RTK solutions. Results for day 19.10.2021 left and day 21.10.2021 right.

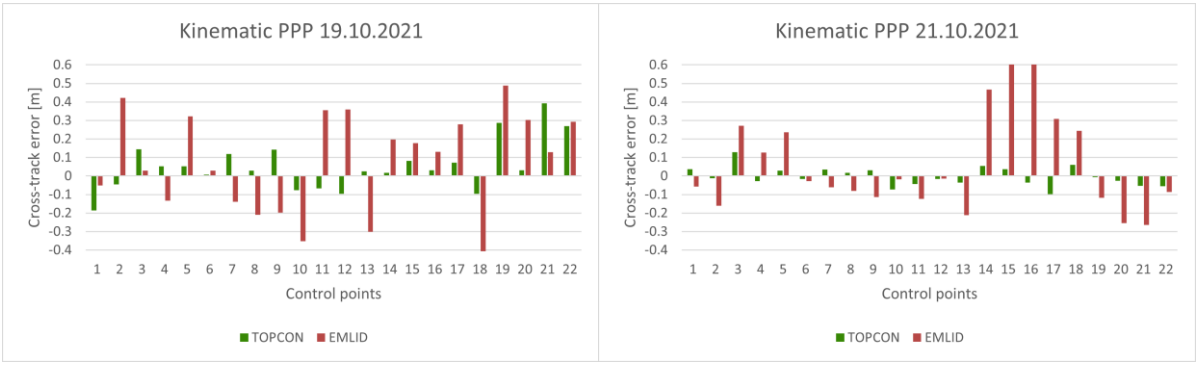

Figure 4. Cross-track errors computed in each control point for the network post-processed PPP solutions. Results for day 19.10.2021 left and day 21.10.2021 right.

Table 5 gives adjusted standard deviations, s_{ct}, for each receiver and kinematic solution.

Table 5. Adjusted standard deviations for cross-track errors, S_{ct}, for each receiver and kinematic solution.

	RTK 19.10.2021	RTK 21.10.2021	PPP 19.10.2021	PPP 21.10.2021
Emlid	0.072 m	0.049 m	0.270 m	0.551 m
Topcon	0.067 m	0.051 m	0.137 m	0.031 m

Along the reference trajectory, the physical obstructions due to buildings, terrain and vegetation, varied from severe to negligible. As expected, the solution status for individual RTK-epochs varied between "fix-solution" and "float-solution" indicating whether carrier phase ambiguities had been fixed to integer values or were estimated as nuisance parameters. We manually inspected the RTK solution statuses and found that all kinematic coordinates used in the computations of cross-track errors, were associated with "fix-solution" flags.

It is generally expected that positional accuracy for kinematic RTK with a fix-solution is at the sub-decimeter level (e.g. Hofmann-Wellenhof et al, 2008). For some control points, the cross-track errors, as given in Figure 3, then appear to be larger than expected. An explanation for the relatively large cross-track errors for the RTK-solutions in some control points, could be a combination of incorrect fixing of the carrier phase ambiguities, weak geometry and severe multipath. Concerning the topic of this paper, it is interesting to notice that for the network RTK-solutions, there are very small differences in cross-track errors between the Emlid and the Topcon receiver.

For the PPP solutions, the cross-track errors from the Topcon receiver are noticeable smaller than for the Emlid receiver. The CSRS-PPP post-processing service uses dual-frequency observations from GPS and GLONASS only. We have already concluded that the Emlid receiver supplies fewer dual-frequency observations for the GPS system than the Topcon receiver. We have also disclosed that carrier phase observations in RINEX-files from the Emlid receiver have missing epochs and that post-processing software might interpret these missing epochs as cycle slips. In PPP processing it is generally difficult to repair cycle slips by bridging successive continuous arcs of carrier phase observations. As a result, corresponding carrier

phase ambiguity parameters are instead reset in the occurrence of a cycle slip. Frequent resetting of carrier phase ambiguity parameters will weaken the overall geometry in a PPP parameter estimation.

We also notice, when comparing RTK- and PPP solutions, that the Topcon receiver has somewhat similar cross track errors. This is especially true for the measurements made on 21.10.2021, while the results from 19.10.2021 are less conclusive. What is clear from the results, however, is that the Emlid receiver has noticeably larger cross-track errors for the PPP-solutions than for the RTK-solutions.

6. CONCLUSIONS

The Emlid receiver has not implemented anti-spoofing technology to track the encrypted P(Y)-code for GPS satellites and therefore supplies fewer GPS dual-frequency observations than the Topcon receiver. In applications that heavily depend on dual frequency GPS-observations, like the CSRS-PPP processing service, the use of observations from the Emlid receiver will give lower accuracy than the use of a high-end GNSS receiver with P(Y)-code tracking capability, like the Topcon receiver. As the GPS-system is being modernized, where new satellites transmitting the L2C-signal replace older satellites, the Emlid receiver will gradually receive dual frequency observations from more GPS satellites.

Carrier phase observations from the Emlid receiver seem to have considerably more cycle slips than carrier phase observations from the Topcon receiver. However, some of the apparent cycle slips in the Emlid data, as seen in RINEX observations files, are likely due to data recording/storage problems and not GNSS-signal tracking problems. In post-processing applications using RINEX-files from the Emlid receiver, these apparent cycle lips, might weaken the solutions.

Based on the analysis of static observations in a geometry-free observation domain, code observations from the Emlid receiver have larger combined errors from multipath and noise than code observations from the Topcon receiver. For kinematic observations observed along a trajectory with varying physical obstructions, combined code multipath- and noise errors from the two receivers are at the same level, except for GLONASS f_2-observations were Emlid performs better than Topcon.

For kinematic measurements in a VRS network-RTK mode using observations from GPS, GLONASS, Galileo and BeiDou, we have disclosed very small differences for cross-track errors between the Emlid- and the Topcon solutions. Utilizing observations from all four GNSS-systems, the overall effect of the previously mentioned drawbacks of the Emlid receiver seems to level out compared to the Topcon receiver. It should, however, be mentioned that different RTK processing engines are used in the two receivers, and that the processing engine in the Emlid receiver might be compensating for the lower quality of raw-data.

For kinematic measurements based on the CSRS-PPP post-processing service, the Topcon solutions have considerably lower cross-track errors than the Emlid solutions.

REFERENCES

Emlid. (2021). https://emlid.com/reachrs2/

Emlid Community. (2021). https://community.emlid.com/t/multi-band-reach-rs2-is-here/13655/114

Estey, L.H. & Meertens, C.M. (1999). TEQC: The Multi-Purpose Toolkit for GPS/GLONASS Data. GPS Solutions, Vol. 3, No. 1.

GPS.GOV. (2021). https://www.gps.gov/systems/gps/modernization/civilsignals/

GPS World. (2019). https://www.gpsworld.com/emlid-launches-reach-rs2-centimeter-accurate-rtk-gnss-receiver/

Hofmann-Wellenhof, B., Lichtenegger, H. & Wasle, E. (2008). GNSS – Global Navigation Satellite Systems. Springer.

IGS. (2021-a). https://www.igs.org/wg/rinex/

IGS. (2021-b). https://www.igs.org/wg/antenna/

Himle, S. (2021). https://github.com/himsve

Kartverket. (2021). https://www.kartverket.no/til-lands/posisjon/hva-er-cpos

Natural Resources Canada. (2021). https://webapp.geod.nrcan.gc.ca/geod/tools-outils/ppp.php?locale=en

Norkart. (2021). https://www.norkart.no/planoggeodata/oppmaling/

Roald, B.E. (2020). Methods for the Performance Evaluation of GNSS Receivers: A Software Development Process. Master's Thesis 2020, Norwegian University of Life Sciences.

Takasu, T. (2011). RTKLIB: An Open Source Program Package for GNSS positioning. http://www.rtklib.com/

Tétreault P., Kouba J., Héroux P. & Legree, P. (2005). CSRS-PPP: an internet service for GPS user access to the Canadian Spatial Reference Frame. Geomatica, 59(1).

Topcon. (2021). https://www.topcon.co.jp/en/positioning/products/pdf/hiper_vr_broch_7010-2258_revb_sm.pdf

u-Blox. (2021). https://www.u-blox.com/en/product/zed-f9p-module

Weston, N.D. & Schwieger, V. (2010). Cost Effective GNSS Positioning Techniques. FIG Publication No 49. FIG Commission 5 Publication. The International Federation of Surveyors, Copenhagen, Denmark.

Lipatnikov, L.A. & Shevchuk, S.O. (2019). Cost Effective Precise Positioning with GNSS. FIG Publication No 74. FIG Commission 5 Publication. The International Federation of Surveyors, Copenhagen, Denmark.

- All internet resources were last accessed on 31.12.2021

BIOGRAPHICAL NOTES

Ola Øvstedal is an Associate Professor at the Department of Geomatics, Faculty of Science and Technology, Norwegian University of Life Sciences. He received his PhD in geodesy in 1991. Current research interest are satellite positioning and estimation techniques. He is a national delegate to FIG Commission 5 "Positioning and Measurements".

Johan Tobias Arnell, Isak Foss Ingebrigtsen and **Simen Walbækken Tangen** are year-4 students at the MSc-program in geomatics at the Department of Geomatics, Faculty of Science and Technology, Norwegian University of Life Sciences.

Bjørn-Eirik Roald graduated with a MSc in geomatics from the Department of Geomatics, Faculty of Science and Technology, Norwegian University of Life Sciences in 2020 and is currently a PhD-student at the Faculty of Science and Technology, Norwegian University of Life Sciences.

CONTACTS

Ola Øvstedal
Section of Geomatics, Faculty of Science and Technology
Norwegian University of Life Sciences
P.O.Box 5003, N-1432 Ås, Norway
Tel: +47 67231549
Email: ola.ovstedal@nmbu.no
Web site: https://www.nmbu.no/en

Johan Tobias Arnell, Isak Foss Ingebrigtsen, Simen Walbækken Tangen
MSc students, Norwegian University of Life Sciences
E-mail: johan.tobias.arnell@nmbu.no
E-mail: isak.foss.ingebrigtsen@nmbu.no
E-mail: simen.walbakken.tangen@nmbu.no

Bjørn-Eirik Roald
PhD student, Norwegian University of Life Sciences
E-mail: bjorn-eirik.roald@nmbu.no